Radiation Measurements 177 (2024) 107246

Contents lists available at ScienceDirect

Radiation Measurements

journal homepage: www.elsevier.com/locate/radmeas

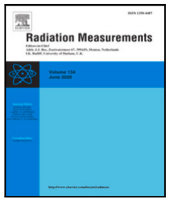

Online and offline Radiation-Induced Attenuation measurements on FD-7 radiophotoluminescence dosimeters irradiated at high X-ray doses

A. Hasan [a,1], Y. Aguiar [a,b], R. García Alía [b], C. Campanella [a,2], A. Morana [a], A.K. Alem [a], S. Girard [a,c], A. Raj Mandal [a], M. Ferrari [a,*]

[a] Université Jean Monnet Saint-Etienne, CNRS, Laboratoire Hubert Curien UMR 5516, Saint-Etienne, F-42023, France
[b] European Organisation for Nuclear Research (CERN), Geneve, CH-1211, Switzerland
[c] Institut Universitaire de France (IUF) Ministère de l'Enseignement Supérieur et de la Recherche, Paris, 75005, France

ARTICLE INFO

Keywords:
Dosimetry
Radiophotoluminescence (RPL)
Radiation-Induced Attenuation (RIA)
X-ray
Transmittance

ABSTRACT

Radiophotoluminescence (RPL) FD-7 glass dosimeters find applications in low to high dose radiation environments. This work presents an experimental characterization of RPL glass dosimeter, irradiated with 100 kV X-ray tubes at room temperature at doses ranging from 1.3 kGy to 0.47 MGy, much higher of their common use range. In this study, a customized set-up has been developed, allowing the online investigation of the glass transmission changes with radiation, known as Radiation-Induced Attenuation (RIA), as well as the recovery and post-mortem characterizations up to 2 months after irradiation. Multi-wavelength analysis was performed, focusing on the range between 200 nm and 800 nm. At 700 nm and 800 nm, RIA increases progressively with dose up to about 5 kGy, and tends to approach saturation (2–3 dB/mm) for doses higher than 50 kGy. Higher attenuation is reported at lower wavelengths: 445-nm light transmission reduces to only about 1% of its initial value after 2 kGy. RIA recovery after irradiation was observed, up to 6% at 700 nm wavelength within 3 h from the irradiation conclusion and up to 26% 2 months after, especially at doses in the kGy range. Both online RIA and its recovery are highly dependent on the selected wavelength and on the total absorbed dose. This information is crucial for the extension of the use of these dosimeters up to high doses, complementary to the RPL signal, traditionally used alone for the determination of doses up to the Gy range.

1. Introduction

Reliable dosimetry systems are essential to characterize radiation environments, aiming at ensuring safety for human operators as well as to minimize the radiation effects on materials, electronics and in general every equipment susceptible to radiation damage. In this context, numerous dosimetry techniques have been developed, targeting specific radiation environments and applications. Radiophotoluminescence (RPL) materials, such as Ag-doped phosphate glasses are extensively used as passive dosimeters and are under permanent development (McKeever, 2022; Knežević et al., 2011). They feature small size, linear response with accumulated dose up to tens of Gy, low energy dependency, reproducibility, non-destructive multiple readout capability and long stability against fading effect (Vincke et al., 2007; Pramberger et al., 2022; Yamamoto, 2011; Huang and Hsu, 2011; Harb et al., 2022; Wesolowska et al., 2017; Yanagida et al., 2022; Knežević et al., 2013; McKeever, 2022; Sholom and McKeever, 2020).

Despite the relevance for many scientific and industrial applications, the use of RPL dosimeters up to high doses, typically in the kGy to MGy range, is less common and still under development. A few studies report data in this range (Vincke et al., 2007; Pramberger et al., 2022; Sholom and McKeever, 2020).

RPL dosimeters, made of FD-7, a Ag-doped phosphate glass, are used at CERN along the accelerator complex, as passive dosimeters. in combination with other radiation monitors such as beam loss monitor (BLM) (Holzer et al., 2012), radiation monitoring (RadMON) (Spiezia et al., 2011) and distributed optical fiber (OF) sensors (Di Francesca et al., 2018), to monitor doses in selected positions of experimental areas (Pramberger et al., 2022; Ferrari et al., 2022; Biłko et al., 2023; Lerner et al., 2023; García Alía et al., 2018) and for the dose monitoring of materials irradiated in external irradiation facilities (Ferrari et al., 2023). Accurate monitoring of the radiation levels is primordial not only for the prevention and maintenance of beam elements against

* Corresponding author.
E-mail address: matteo.ferrari@univ-st-etienne.fr (M. Ferrari).
[1] Now at nanoCaps AS, Vestfold Innovation Park, Raveien 205, 3184 Borre, Norway.
[2] Now at EXAIL PHOTONICS, 3 Rue Sophie Germain, 25000 Besan00E7on, France.

https://doi.org/10.1016/j.radmeas.2024.107246
Received 28 February 2024; Received in revised form 3 June 2024; Accepted 16 July 2024
Available online 20 July 2024

material damage, but also to cope with radiation effects on electronics systems (Aguiar et al., 2021). For the readout of these RPL dosimeters, CERN has developed a system that employs a dual-channel measurement set-up, combining Radiation-Induced Attenuation (RIA) and RPL measurements and strategically extending the dynamic range of the RPL dosimeters to high-level dose, as the ones available in the accelerator complex. A comprehensive description of this measurement methodology is presented in previous works (Pramberger et al., 2022; Vinke and Trummer, 2014). Two main macroscopic radiation effects in RPL glasses can in fact be observed. Radiation-induced free electron–hole pairs produced in the glass are captured by the Ag^{+} ions already present in the glass, generating RPL centers. They can be then excited by UV light and the following relaxation results in the emission of a visible light, that determines the RPL signal (Kurobori et al., 2010; Miyamoto et al., 2011; Okada et al., 2023; McKeever, 2022). The integrated radiophotoluminescence signal is generally agreed to be proportional to the dose up to about 10 Gy (Okada et al., 2023; Yamamoto, 2011), but recent studies suggest that the behavior could saturate at much higher doses of 1 kGy or 10 kGy (McKeever, 2022; Sholom and McKeever, 2020), depending on the specific RPL center. The scientific community seems to still lacks consensus on the nature and of the exact kinetics of the RPL centers, this being especially true at doses in the kGy range, where data are scarce.

Traditionally, RPL signal is used alone for dose determination up to 10 Gy, which is of general interest for medical applications, and personal and environmental dosimetry (McKeever, 2022). Additionally, radiation induces an increase in the light attenuation through the sample, corresponding to a transmittance decrease, mainly due to the generation of optically active point defects (color centers) and related absorption bands (Girard et al., 2013). This second effect, associated to a macroscopic glass darkening, becomes particularly relevant at higher doses, in the kGy–MGy range, while at lower doses the irradiated glass remain overall transparent (Pramberger et al., 2022; Ferrari et al., 2024). The decrease in the transmission capability is generally referred to as Radiation-Induced Attenuation (RIA), and it is one of the most common radiation effects in photonics components, such as optical fibers (Girard et al., 2018b) and bulk optical materials (Allanche, 2020; Girard et al., 2018a). Transmittance at 445 nm is used as a complementary information for the determination of doses higher than 300 Gy with RPL dosimeters in CERN's system (Pramberger et al., 2022).

The RPL dosimeters used at CERN and irradiated in this work are the FD-7 glass rod elements that are part of commercial GD-301 dosimeters. They are typically deployed in the vicinity of the accelerator beam elements of interest before operation. Their retrieval and consequent measurement after operation and accelerator shut-down are subject to the radiation protection constraints related to the activation of both the accelerator elements and the dosimeters themselves. Consequently, and depending on the specific operation schedule of the accelerator complex, the dosimeter readout is usually delayed by several weeks after the operation end. The behavior of the RPL dosimeters during and immediately after irradiation is not assessed, and the information on the on-line dosimeter response cannot be investigated.

Various already existing set-ups allow the online evolution of different types of glass samples to be measured as a function of the dose (McKeever et al., 2020; Okada et al., 2023, 2021; Girard et al., 2018a; Kurobori, 2018). For example, a system for the measurement of the RPL signal under X-ray irradiation was developed in Okada et al. (2023, 2021); a set-up for RIA measurements in bulk glass samples in the so called 'free-space' optic configuration was developed in Girard et al. (2018a); and online systems for RPL signal measurement in which an RPL dosimeter is linked to an optical fiber for signal transmission were developed by Kurobori (2018) and McKeever et al. (2020). Inspired by these systems, an adapted set-up is described in the present paper, developed specifically to target the online RIA measurement in RPL dosimeters.

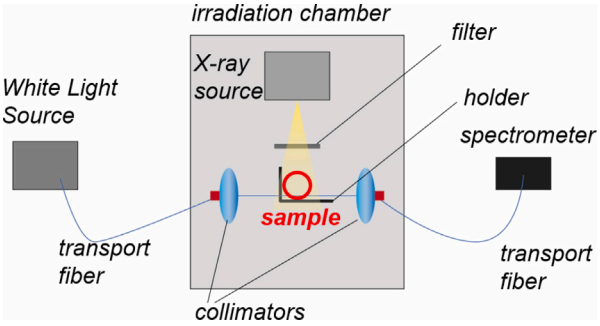

Fig. 1. Schematic diagram of the developed set-up for RIA measurements on RPL samples. The main elements are highlighted.

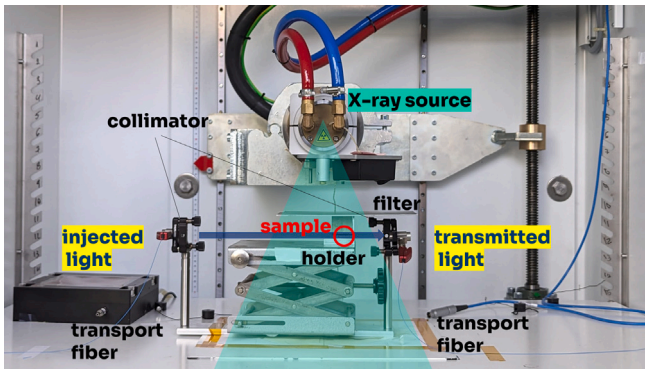

Fig. 2. Picture of part of the set-up placed inside X-ray irradiator chamber for RPL online measurements. While the sample itself may not be discernible due to its small size, its position is highlighted by the red circle. The radiation cone emitted by the source is pictorically represented by a pale blue triangle. The passage of the light in free space and through the sample between the two collimators is represented by a blue arrow.

This study presents a methodology to measure RIA in RPL FD-7 glass rods irradiated with a commercial X-ray tube up to doses in the MGy range. Both online and offline characterizations are reported, including a multi-wavelength attenuation analysis (spectral RIA), and relative transmittance decrease during irradiation. Post-irradiation measurements allow the kinetics of possible unstable defects at room temperature to be followed after irradiation. The performed tests aim at broadening the knowledge of RPL dosimetry, with a special focus on RIA, whose analysis seems promising for the extension of the dosimeter range and for the possible applications of this technique.

2. Materials and methods

2.1. Samples

FD-7 glass rods of GD-301 RPL dosimeters commercialized by Chiyoda Technology (Japan) are used in the described experiments. FD-7 samples are Ag-doped phosphate glasses produced in the form of cylindrical rods, with a diameter of 1.5 mm and length of 8.5 mm. The composition of the glass is: P: 31.55 wt%, O: 51.16 wt%, Al: 6.12 wt %, Na: 11% and Ag: 0.17% (Pramberger et al., 2022; McKeever, 2022). GD-301 dosimeters normally include a plastic container in which the FD-7 glass rod is embedded. For the experiments here described, the glass rod is removed from the dosimeter, and the plastic container is not used. In the present work, the term RPL dosimeter is used to indicate the FD-7 glass rod alone.

2.2. Experimental set-up

In a traditional RIA online measurement, the signal attenuation through the sample is measured while the sample is irradiated and

after irradiation. This allows the RIA kinetics to be monitored during and after irradiation, providing key information about the competition between the generation and bleaching mechanisms of defects during the exposure and the recovery mechanism, if any, after the irradiation conclusion.

The fundamental experimental setup for RIA measurements consists of three elements: a light source (either white, or monochromatic), a radiation source (gamma-rays, X rays, etc.) and a detector (spectrometer, photodiode, etc.). The transmitted light intensity is recorded before, during and, often, after irradiation.

This type of configuration offers satisfactory performance in terms of dynamic range. Spectral measurements are generally preferred to monochromatic RIA growth kinetics, as they are more informative on the investigated radiation effects and basic mechanisms (Di Francesca et al., 2019).

A customized set-up, whose scheme is shown in Fig. 1, has been developed in the present work to perform both online and post-irradiation characterizations. Light is transmitted through the FD-7 sample longitudinally at multiple wavelengths simultaneously and collected afterwards. To measure spectral RIA, a DH-2000 Deuterium-Halogen light source from Ocean Optics, simply referred to as White Light Source (WLS), is used. QE-Pro 38011 from Ocean Optics, a high-resolution spectrometer, has been used to detect the transmitted light from around 240 nm to 1000 nm.

Light is injected in the sample in a free-space configuration, as shown in Fig. 2. Light is at first guided through a pure silica core fiber (with high OH contents for optimized transmission in the UV–visible domains) from the WLS to the metal coated mirror, working as a light collimator. The collimated light beam passes through the dosimeter, placed on a dedicated holder as shown in Fig. 3. The transmitted light is then collected by a second collimator identical to the previous one and transferred to the spectrometer using a second transport optical fiber of the same type. The specific shape of the transmitted spectrum depends on the light source and on the guiding medium. However, it does not affect the RIA measurements, as they are relative measurements.

For online RIA measurements, the sample, the sample holder, whose design is further described in Section 2.3 and the collimators are placed inside the X-ray irradiation chamber, while the WLS and spectrometer are connected to the collimators from the outside of the irradiation chamber through the transport fibers. Additionally, a 1.5 mm Al filter was placed between the source and the sample to harden the X-ray spectrum and improve the dose homogeneity across the sample volume, as discussed in Ferrari et al. (2024) and as summarized in Section 2.5.

2.3. Sample holder

A custom sample holder, as shown in Fig. 3, was designed to have the following features:

- the beam size of the transmitted light has to be smaller than the diameter of the RPL sample, so that the signal received by the spectrometer includes only the light that actually passed through the sample. The holder wall has 1.0 mm diameter aperture to filter out the excess light.
- the correct alignment of the cylindrical RPL dosimeter in respect to the aperture is granted by the 1.52 mm × 0.76 mm groove, making the positioning more precise and efficient and ensuring a better measurement repeatability. Intensity measurements performed by positioning the same dosimeter in the holder several times showed a standard deviation between repeated measurements below 5%.
- the holder is entirely made of aluminum, making it radiation tolerant and compatible with temperature control to be achieved in future experiments via heating or cooling plates.

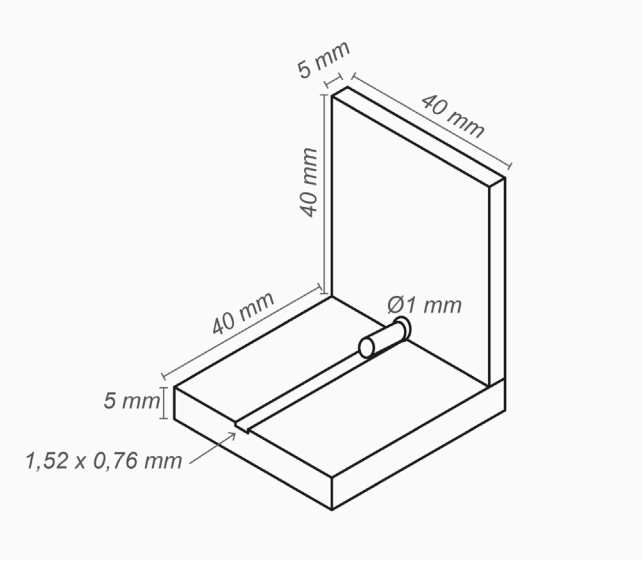

(a)

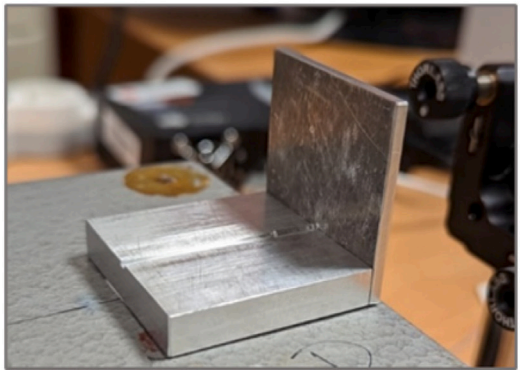

(b)

Fig. 3. Design concept of the sample holder integrated with a filter featuring a 1.0 mm diameter aperture: (a) schematic with detailed dimensions and (b) photograph of the fabricated sample holder used in the experimental setup.

2.4. Radiation induced attenuation

The developed set-up allows radiation-induced variations of the light signal transmitted through the sample to be measured.

The experiments described in the present paper are based on the RIA measurements performed on optical fiber samples, as reported in Di Francesca et al. (2018), Girard et al. (2019), Morana et al. (2020), and on RIA measurements performed on bulk glasses (Allanche, 2020).

RIA can be computed at any time of the experiment corresponding to signal acquisition using Eq. (1), (Allanche, 2020):

$$RIA\,(t,\lambda) = -\left(\frac{10}{L}\right)\cdot \log_{10}\left(\frac{I(t,\lambda) - I_N(\lambda)}{I_{ref}(0,\lambda) - I_N(\lambda)}\right) \quad (1)$$

Where $I_{ref}(0,\lambda)$ and $I(t,\lambda)$ are the intensity of the signal transmitted through the sample before irradiation start and at a specific time t during or after irradiation, respectively, at a specific wavelength λ.

$I_N(\lambda)$ is the background signal due to thermal noise at a specific wavelength λ.

$I_{ref}(0,\lambda)$, $I(t,\lambda)$ and $I_N(\lambda)$ are absolute intensities expressed in photon counts over an integration time specified by the user.

L is the sample length.

RIA generally depends on dose, dose rate, wavelength, temperature, type and energy spectrum of radiation, composition of materials, injected light power etc. (Girard et al., 2013, 2019).

RIA as calculated using Eq. (1) can be referred to using three different names depending on the set-up and irradiation conditions in which the measurement of $I_{ref}(0, \lambda)$ and $I(t, \lambda)$ is performed.

2.4.1. Online RIA

When $I(t, \lambda)$ is measured during irradiation, the quantity calculated using Eq. (1) is referred to as online RIA. Online RIA values are presented as a function of the absorbed dose and can be calculated for any sampled intermediate time value up to the total irradiation time, corresponding to the total absorbed dose.

One of the advantages of online RIA measurement is that it allows identifying the possible presence and evolution of optical absorption bands associated to the induced defects as a function of the dose. This is not necessarily achievable through post-irradiation measurements alone, traditionally performed on passive RPL dosimeters, in which mostly stable defects will be detected, and therefore highlights the importance of this study.

2.4.2. Recovery

Measurement of $I(t, \lambda)$ might be carried on beyond irradiation conclusion, typically for some hours immediately following irradiation and using the same set-up and leaving the sample and the instrumentation in exactly the same configuration. This measurement provides information on the recovery processes that depend on the evolution of the radiation-induced metastable defects in the sample material with time.

Competitive build-up and recovery processes can lead to RIA increases or decreases, respectively, after irradiation, in correspondence of specific absorption bands. RIA generally stabilizes to an equilibrium after a certain post-irradiation time, depending on the temperature and on other environmental conditions (Girard et al., 2013, 2019; McKeever et al., 2020). When $I(t, \lambda)$ is measured immediately after irradiation conclusion, typically for some hours, the RIA calculated using Eq. (1) is referred to as Recovered RIA or simply Recovery. Recovery values are presented as a function of time starting from irradiation conclusions. They can be normalized to the Online RIA value measured at the very end of the irradiation to appreciate the relative RIA variations as a function of recovery time.

In the experiments here presented, recovery measurements were performed for about 3 h starting from the irradiation conclusion.

The recovery kinetics is highly dependent on the nature of the point defects responsible for the RIA at the considered wavelength and in particular to its thermal and photo stability.

2.4.3. Post-mortem

Measurement of $I(t, \lambda)$ might be performed on irradiated samples, typically from few days up to several months after irradiation conclusion. Post-mortem measurements are realized out of the irradiation chamber, in a set-up configuration similar to the ones showed in Fig. 3(b).

For post-mortem measurement, a different pristine (unirradiated) RPL sample is used as reference for the determination of the initial intensity $I_{ref}(0, \lambda)$. Single measurements of $I(t, \lambda)$ are performed at selected time intervals after irradiation, for example 14 days or 2 months after irradiation. In these conditions, the quantity calculated using Eq. (1) is referred to as Post-mortem RIA.

In the described experiments, samples were stored at uncontrolled room temperature and ambient light conditions after irradiation. Repeated measurements performed on various pristine samples confirmed the repeatability of the measurements and the homogeneity between different pristine RPL samples within 10% variation.

Post-mortem measurements allow the RIA kinetics to be followed over longer time scales, aiming at observing stabilization of attenuation phenomena over time and fading.

Table 1
Summary of the irradiation campaign aiming to assess different dose effects at constant dose rate. (Ferrari et al., 2024).

Sample	D_{RPL} [kGy]	t_{irr}
D1	1.3	10 min
D2	12.9	99 min 40 s
D3	77.7	10 h
D4	466	60 h

2.5. Irradiation conditions

X-ray tubes emit photons across a spectrum of energies, extending up to the maximum energy of the electrons striking the target material, in this case corresponding to 100 keV (Meyer et al., 2023). Photons with lower energy in this spectrum are highly attenuated by the sample thickness, depositing most of their energy on the sample top layers and leading to a highly inhomogeneous dose distribution, as evidenced by Monte Carlo calculations performed in a previous study (Ferrari et al., 2024). The introduction of a 1.5 mm thick Al shielding was proven to effectively harden the X-ray energy spectrum and significantly enhance dose homogeneity across the RPL volume. Therefore, for each irradiation, a 1.5 mm Al filter has been placed between the X-ray source and sample, at a distance of 3 cm from the sample, as shown in Fig. 2.

In the present work, four FD-7 samples were irradiated using the MOPERIX X-ray facility available at Laboratoire Hubert Curien, France. The source has a tungsten target, and the X-ray tube operated at a 100 kV voltage, and at the maximum available current of 45 mA. All the samples were irradiated in the same configuration, at a constant dose rate of 0.58 Gy[H_2O]/s, at uncontrolled room temperature, and for a total duration ranging from 10 min to a maximum of 60 h of continuous irradiation. The temperature at the sample position was monitored during irradiation with thermocouples placed in contact with the sample holder. Temperature varied between a minimum of 23 °C and a maximum of 28 °C in the performed irradiations.

2.6. Dosimetry

Dose rate to water $\dot{D_W}$ at the sample position was measured using a PTW ionization chamber 2334. The readout, corresponding to 0.58 Gy[H_2O]/s, was used to plan the irradiation campaigns. In a previous study, Ferrari et al. (2024) determined a conversion factor C_{sim} allowing the readout of the ionization chamber to be converted in dose to RPL material D_{RPL} in these irradiation conditions. C_{sim} corresponds to 3.7 ± 0.9 (Ferrari et al., 2024). In this work, all the used dose values refer to dose to RPL material, and they are obtained with the following formula:

$$D_{RPL} = \dot{D_W} \cdot t_{irr} \cdot C_{sim} \quad (2)$$

where t_{irr} is the total irradiation time.

A readout of the dosimeters was performed at CERN about six weeks after irradiation, providing experimental dose values comparable with the expected ones within 10% for D2–D4 samples, and within 20% for D1, as discussed in Ferrari et al. (2024).

Information on the irradiation campaign are reported in Table 1, along with the D_{RPL} values, and the irradiated RPL samples are shown in Fig. 4.

For the four samples D_{RPL} varied from 1.3 kGy to 0.47 MGy. An overall uncertainty of ±30% is attributed to total doses, as discussed in Ferrari et al. (2024). The main source of this uncertainty is the inhomogeneity of the dose deposited across the sample volume, determined by the photon attenuation by the sample thickness.

3. Results and discussion

3.1. Online transmitted signal measurements

During irradiation, the color of the FD-7 sample progressively changed, as show in Fig. 4. As the total dose increases, the sample

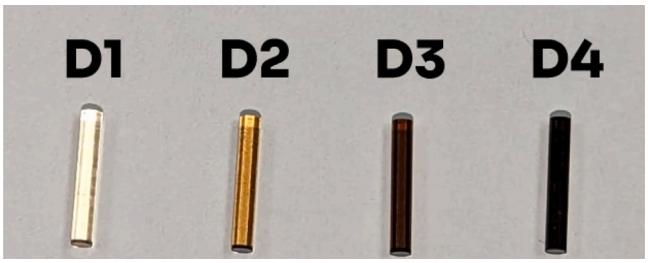

Fig. 4. Irradiated RPL samples D1, D2, D3 and D4. It is evident the darkening mechanism induced by the absorbed dose and the consequent formation of color centers in the glass.

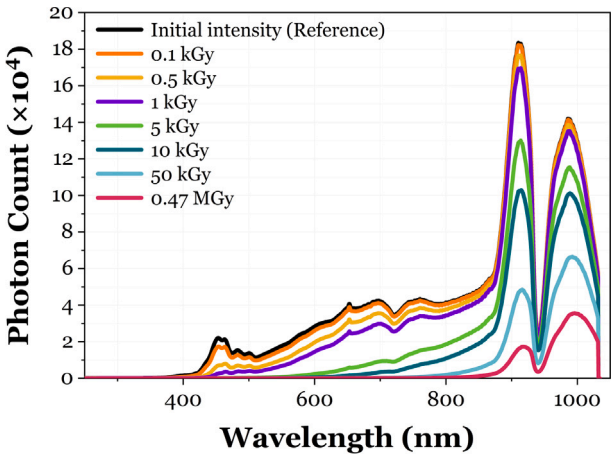

Fig. 5. Online Transmitted intensity through D4 sample as a function of the wavelength for selected dose values.

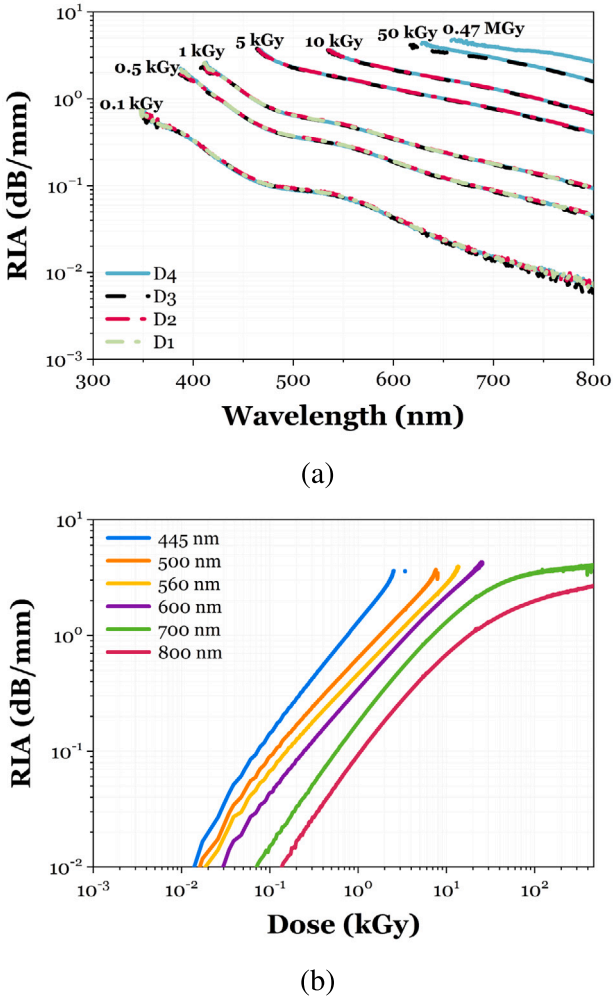

Fig. 6. (a) Spectral online RIA measured at different dose levels, as a function of wavelength, for samples D1–D4; (b) Online RIA kinetics as a function of absorbed dose at some specific wavelengths during irradiation for sample D4.

becomes progressively darker. The darkening of the sample with increase in deposited dose is a macroscopic indication of the increase in the number of color centers with dose.

In Fig. 5(a), an example of reference spectral transmitted signal $I_{ref}(0, \lambda)$, expressed in total photon count as recorded with the spectrometer, is reported as a function of the wavelength (black curve). In all the reported measurements, the wavelength range is selected between 300 nm to 800 nm, as signals out of this wavelength range have intensities comparable to noise level. High OH transport fibers are responsible for the observed absorption peak around 920 nm. Transmitted signals $I(t, \lambda)$ sampled in correspondence to selected intermediate dose values ranging from 0.1 kGy to the maximum dose of 0.47 MGy are shown. As the total absorbed dose increases, the intensity of the transmitted spectrum progressively reduces. Attenuation is highly dependent on the considered wavelength, experiencing greater attenuation with dose at shorter wavelengths. The light absorption increases with dose as the number of color centers, acting like absorption centers.

3.2. Online RIA measurements

Spectral online RIA as a function of wavelength for representative dose values of the four irradiated samples is shown in Fig. 6(a). RIA progressively increases with total absorbed dose at all wavelengths, and exhibits higher values at lower wavelengths.

The RIA growth of all the four samples at same dose levels and at same wavelengths superimpose, evidencing the repeatability of the measurement. Accordingly, Fig. 6(b) D4 alone is reported as representative of the four samples.

At least two absorption bands are visible in Fig. 6(a). Peaks of those bands seem to be located around 550 nm and around 380 nm. The contribution to the total RIA of the absorption peak around 550 nm wavelength exhibits gradual reduction with increase in total dose.

These bands might be associated to the activation of precursor sites in limited number, that are efficiently generated at the beginning of irradiation and that are the main contributor to RIA around 550 nm. As the dose increases and when the generation of these defects saturates, the contribution to RIA decreases up to the point that it became negligible compared to the ones associated to different defect types. Similar phenomena are observed in irradiated optical fibers (Girard et al., 2013; Morana et al., 2020).

The origin of these absorption bands cannot be identified with RIA measurement alone, and its systematic investigation is beyond the scope of the present work. However, in the literature, the 550 nm absorption band is suggested to be related to the Phosphorous Oxygen Hole Centres (POHC) (Dmitryuk et al., 1989; Yokota and Imagawa, 1967; McKeever et al., 2019). POHC centers are formed when h^+ holes are trapped by the PO_4^{3-} tetrahedra sites, which are elemental constituents of the network structure of phosphate glasses, via the following mechanism (McKeever et al., 2019):

$$h^+ + PO_4^{3-} \rightleftharpoons POHC \quad (3)$$

On the other hand, the absorption band around 380 nm is suggested to be associated with the Ag^0 centers, produced when free electrons,

produced by radiation, are captured by the Ag^{+} ions present in the glass dosimeters (Miyamoto et al., 2011; McKeever et al., 2019). Complementary analyses such as RPL and EPR measurements could help precisely identifying their origin and their kinetics.

RIA kinetics is plotted in Fig. 6(b), as a function of the absorbed dose at six selected wavelengths: 445 nm (the wavelength used at CERN to identify different dose ranges (Pramberger et al., 2022)); 500 nm, 560 nm, and 600 nm (near to the absorption band) 700 nm and 800 nm. RIA at all the analyzed wavelengths increases progressively with absorbed dose, and is higher at lower wavelengths. For values higher than approximately 3 dB/mm, the intensity of measured signal becomes comparable to the noise, and accordingly, the RIA measurement cannot be reliably determined.

At 700 nm and 800 nm, the RIA increases monotonically as a function of the dose with a power-law behavior up to approximately 10 kGy, and then it tends to reach a saturation for doses higher than about 50 kGy. At 445 nm RIA increases progressively up to approximately 2 kGy, corresponding to the maximum measurable value. RIA saturation indicates that the number of color centers stabilizes.

3.3. Recovery measurements

In Fig. 7(a), spectral online RIA for all the four samples at the end of the irradiation is compared with Recovery after three hours from the irradiation end. The difference between solid lines and dashed lines at each dose level shows the RIA variations in this time range. Transmission window decreases as dose increases, being the narrowest for D4 sample. At 0.47 MGy in fact, as reported in Fig. 6, most wavelengths are not measurable anymore with our set-up and dosimeter length.

For the samples irradiated at the highest doses (D3 and D4), and for which the highest RIA is reported, recovery was comparatively lower and almost not measurable. D1 and D2 samples showed higher recovery, mostly in the wavelengths ranging from about 450 nm to 650 nm.

Normalized recovery kinetics of all the samples at 700 nm wavelength is reported in Fig. 7(b) for comparison. Recovery looks higher and faster at lower doses in the kGy range, while it decreases at higher doses. For instance, at 700 nm wavelength D4 sample shows only 1% of recovery over 2 h 30 min where D1 sample shows a recovery of 1% within 15 min reaching around 6% after 3 h of recovery. The possible reason is that longer irradiation time is necessary to reach higher doses at constant dose rate, and accordingly metastable defects get enough time to stabilize during irradiation. As a result, the remaining defects at higher doses are permanent ones.

Recovery at 445 nm and 550 nm is reported in Fig. 7(c). At these wavelengths, RIA at the end of irradiation is still measurable for D1 samples only. A 6 % recovery is observed at 445 nm, similar to the one observed at 700 nm wavelength at the same dose. By contrast, a much higher RIA recovery is observed at 550 nm, exceeding 25% in about 3 h after irradiation.

It is interesting to note that recovery is particularly relevant in correspondence with the same wavelengths at which one of the absorption bands is located, at about 550 nm. This finding is in agreement with the hypothesis that this absorption band is associated with the POHCs, which are unstable at room temperature and therefore release the trapped holes after irradiation, as described by the reversible Eq. (3). McKeever et al. (2019) studied the evolution of the optical absorption in the same RPL samples at various wavelengths. The irradiation was performed in different conditions and at different dose levels, and the used set-up differs from the one here presented. The developed set-up was not intended to be used for absolute measurements in the present work, however it is interesting to note that McKeever et al. (2019) observed a similar decrease of the normalized absorbance at 550 nm of 6% after irradiation at 720 nm, confirming the trend here reported.

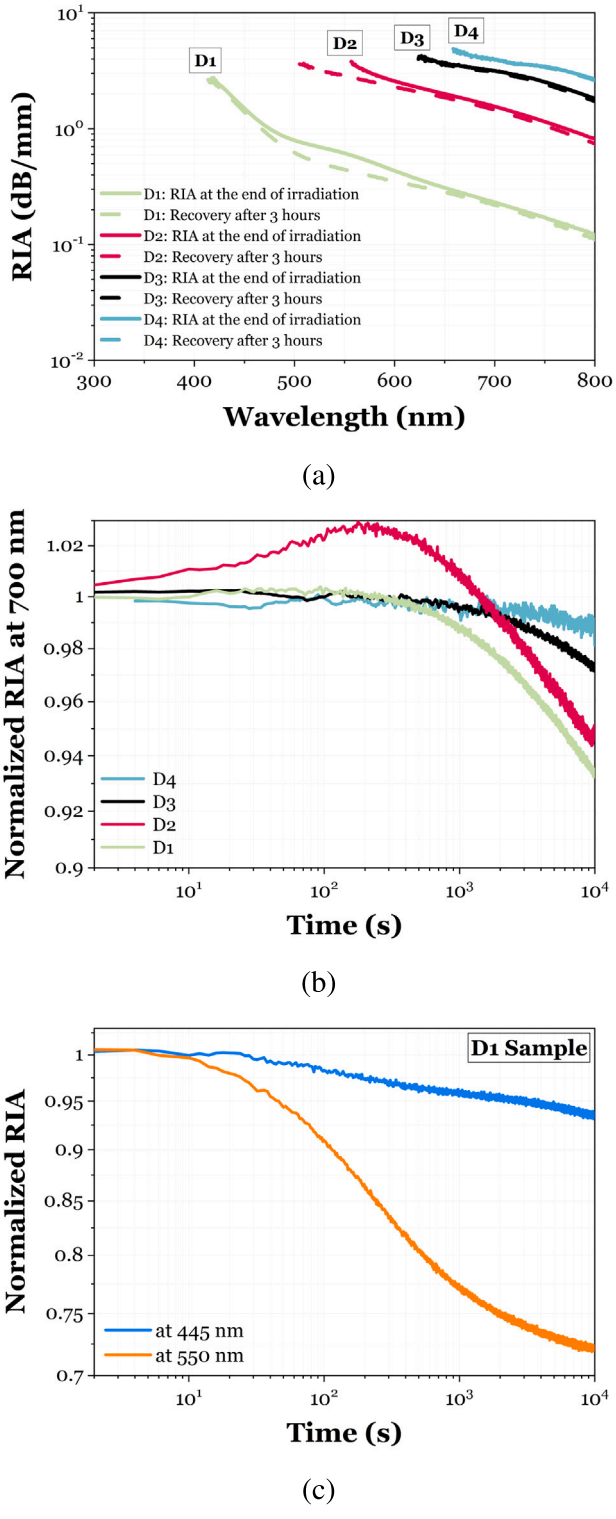

Fig. 7. (a) Spectral online RIA at the end of irradiation and recovery after 3 h. Normalized RIA (b) at 700 nm and (c) at 445 nm and 550 nm wavelengths as a function of time after irradiation.

3.4. Post-mortem measurements

Two post-mortem measurements were realized on the described set of samples. D2, D3, D4 were measured 14 days after the irradiation conclusion and all the samples were measured 2 months after the irradiation conclusion. Results are shown in Fig. 8.

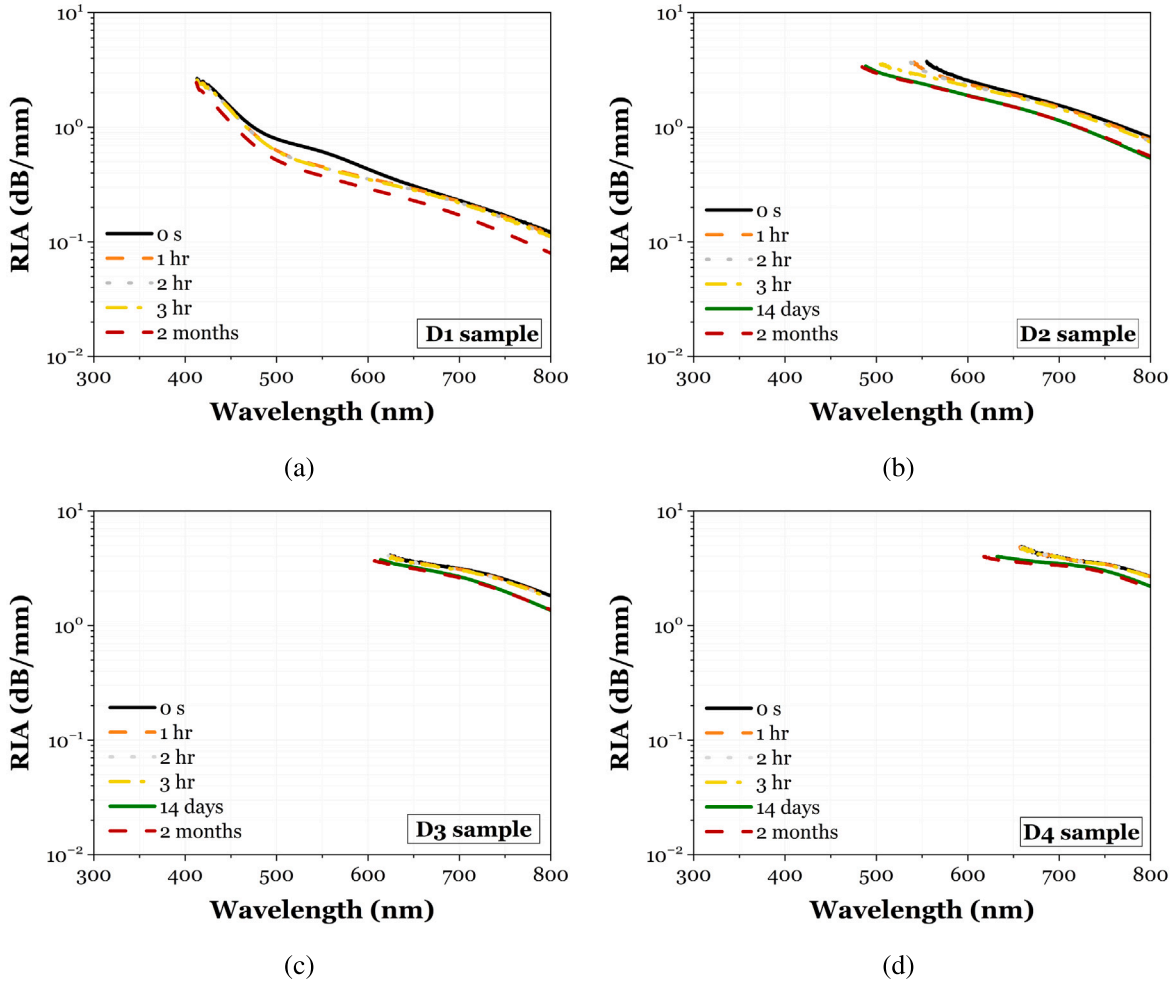

Fig. 8. Comparison of online RIA at the end of irradiation (continuous black line) with Recovery up to 3 h following irradiation and post-mortem measurements measured after 14 days for samples D2–D3 and up 2 months for samples (a) D1, (b) D2, (c) D3 and (d) D4.

Significant RIA decrease is observed after 14 days from irradiation end (0 s in Fig. 7) for all the tested samples at all wavelengths before saturation is reached. For example, for D1 sample at 445 nm a total RIA recovery of about 26 % is reported after 2 month from irradiation. A similar recovery value is observed at 700 nm as well. This recovery value increases up to 39 % at around 550 nm.

Post-mortem RIA after 14 days and 2 months overlap at all wavelengths for D2, D3 and D4 samples, suggesting that saturation and defect stability at room temperature is reached within 14 days after irradiation.

3.5. Relative transmission

The presented set-up was not intended to perform absolute transmission measurements in the present work. However, aiming at a comparison with previous studies, the following formula can be used to calculate relative transmission variations during irradiation:

$$T_R\,(t,\lambda) = \frac{\mathrm{I}(t,\lambda) - \mathrm{I_N}(\lambda)}{\mathrm{I_{ref}}(0,\lambda) - \mathrm{I_N}(\lambda)} \tag{4}$$

Online T_R values are reported as function of the dose for selected wavelengths in Fig. 9. At 445 nm, T_R is reduced to 10% of its initial value at 0.9 kGy and to 1% of its initial value at 2 kGy.

The presented results can be compared with the ones collected by Pramberger et al. (2022) on the same RPL dosimeters. Using a different set-up, Pramberger et al. (2022) reported a transmission decrease to 10% of its reference value at 445 nm at doses ranging between 0.89 kGy and 1.8 kGy, and a decrease to 1% at about 2.7 kGy.

As further discussed in Sections 3.3 and 3.4, online and passive post-irradiation results might not be directly comparable due to recovery phenomena. In fact, in the experiment reported in this study, in the kGy range at 445 nm, RIA recovered up to 26% of the value at the end of irradiation after 2 months from the irradiation conclusion.

Despite the different irradiation conditions in terms of radiation quality, dose rate, measurement time in comparison to irradiation (online vs offline), overall comparable results are found.

4. Summary and conclusions

The study presents a characterization of commercial FD-7 glasses used as RPL dosimeters during and after X-ray irradiation. A new customized setup was developed, enabling online multi-wavelength RIA measurement and its evolution after irradiation.

An experimental campaign was realized irradiating dosimeters in a specific set of irradiation conditions at high doses ranging between 1.3 kGy and 0.47 MGy, a range rarely explored using X-ray irradiation and so far lacking online investigations. Transmitted signal was monitored for the entire irradiation time and for three hours following irradiation for RIA and recovery assessment. Samples were followed-up for two months after irradiation.

The RIA dependency on the absorbed dose and on the wavelength was assessed in a specific set of irradiation conditions. RIA increases

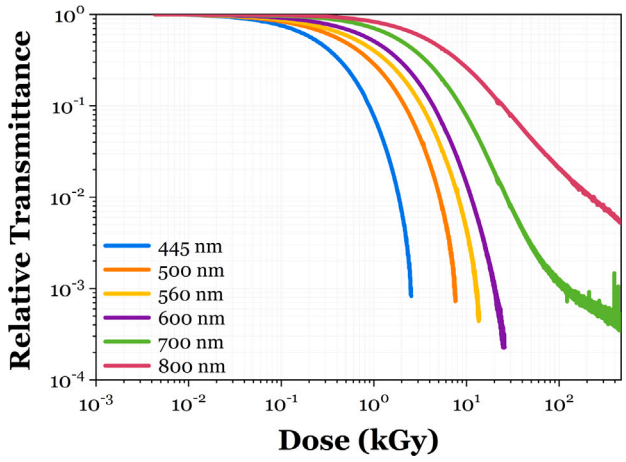

Fig. 9. Relative transmittance T_R as a function of absorbed dose at selected wavelengths for sample D4.

with dose for all the investigated wavelengths, having higher values at lower wavelengths.

Apart from providing information on the spectral RIA as a function of the dose, the outcomes of the study are particularly relevant for high dose applications of these RPL dosimeters. In this range, the transmitted signal is indeed utilized, complementing the traditionally used RPL signal, to determine the absorbed dose.

Recovery kinetics should in fact be accounted for when comparing online measurements with passive readout systems. The recovery observed 14 days and 2 months after irradiation potentially impacts the accurate readout of the dosimeters, currently based on a calibration performed 26 days after 60-Co irradiation. Delays between irradiation conclusion and readout need to be taken into account, especially when this time cannot be easily standardized. This is the case of CERN, where passive RPL dosimeters are generally read weeks to months after irradiation conclusion, in many cases after prolonged exposure to uncontrolled ambient light and temperature conditions. This is common to many other facilities, in which the accessibility of experimental areas limits the retrieval and readout of the dosimeters due to radiation protection and technical constraints. Further recovery and post-mortem investigations would provide useful insights on the possibility of using RPL FD-7 glass dosimeters for online dosimetry as well, especially for doses exceeding the kGy.

This study paves the way for new and broader developments of the dosimetry system currently in use for high doses, possibly integrating transmittance information at multiple wavelengths to enhance dosimetry accuracy in this range, mitigate current method limitations and extend the system sensitivity at higher doses.

Future works will focus on the dependency of spectral RIA and recovery phenomena on dose rate and temperature, which could greatly impact recovery phenomena. Ultimately, the developed methodology together with this first set of results provides insights and prospects for extending RPL dosimeter applications in a wide range of domains beyond particle accelerators, like space, nuclear technology, irradiation facilities and medical physics, where high level doses up to kGy and MGy levels are available and need to be monitored.

CRediT authorship contribution statement

A. Hasan: Writing – original draft, Methodology, Investigation, Formal analysis, Data curation, Conceptualization. **Y. Aguiar:** Writing – review & editing, Validation, Supervision, Resources, Methodology, Data curation, Conceptualization. **R. García Alía:** Writing – review & editing, Validation, Supervision, Resources. **C. Campanella:** Supervision, Methodology, Formal analysis, Data curation. **A. Morana:** Writing – review & editing, Validation, Methodology, Formal analysis, Data curation, Conceptualization. **A.K. Alem:** Software. **S. Girard:** Writing – review & editing, Validation, Supervision, Resources, Project administration, Methodology, Funding acquisition, Data curation, Conceptualization. **A. Raj Mandal:** Data curation, Investigation, Writing – review & editing. **M. Ferrari:** Writing – review & editing, Validation, Supervision, Resources, Project administration, Methodology, Investigation, Funding acquisition, Data curation, Conceptualization.

Declaration of competing interest

The authors declare that they have no known competing financial interests or personal relationships that could have appeared to influence the work reported in this paper.

Adriana Morana is an Associate Editor for a Special Issue in the Transactions of Nuclear Science journal, associated with the ANIMMA 2023 Conference and was not involved in the editorial review or the decision to publish this article.

Matteo Ferrari is a Guest Editor for Lubricants of MDPI and was not involved in the editorial review or the decision to publish this article.

Sylvain Girard is an Editor in Chief of the Sensing and Imaging section of MDPI and Associate Editor of Nature Scientific Reports and was not involved in the editorial review or the decision to publish this article.

Data availability

Data will be made available on request.

References

Aguiar, Y., et al., 2021. Radiation to electronics impact on CERN LHC operation: Run 2 overview and HL-LHC outlook. In: 12th Int. Part. Accel. Conf.. pp. 80–83. http://dx.doi.org/10.18429/JACoW-IPAC2021-MOPAB013.

Allanche, T., 2020. Effect of High Radiation Doses (MGy) On Light Emitting Diodes and Optical Glasses (Ph.D. thesis). Université de Lyon.

Biłko, K., et al., 2023. CERN super proton synchrotron radiation environment and related radiation hardness assurance implications. IEEE Trans. Nucl. Sci. 70 (8), 1606–1615. http://dx.doi.org/10.1109/TNS.2023.3261181.

Di Francesca, D., et al., 2018. Distributed optical fiber radiation sensing in the proton synchrotron booster at CERN. IEEE Trans. Nucl. Sci. 65 (8), 1639–1644. http://dx.doi.org/10.1109/TNS.2018.2818760.

Di Francesca, D., et al., 2019. Implementation of optical-fiber postmortem dose measurements: A proof of concept. IEEE Trans. Nucl. Sci. 67 (1), 140–145. http://dx.doi.org/10.1109/TNS.2019.2946583.

Dmitryuk, A., Paramzina, S., Savvina, O.C., Yashchurzhinskaya, O., 1989. Nature of radiophotoluminescence centers in silver-activated phosphate glasses. Opt. Spectrosc. 66 (5), 626–629.

Ferrari, M., et al., 2022. Design development and implementation of an irradiation station at the neutron time-of-flight facility at CERN. Phys. Rev. Accel. Beams 25, 103001. http://dx.doi.org/10.1103/PhysRevAccelBeams.25.103001.

Ferrari, M., et al., 2023. "Radiation to materials" at CERN. IEEE Trans. Nucl. Sci. 70 (8), 1580–1586. http://dx.doi.org/10.1109/TNS.2023.3241785.

Ferrari, M., et al., 2024. Characterization of radiophotoluminescence dosimeters under X-ray irradiation at high doses. IEEE Trans. Nucl. Sci. http://dx.doi.org/10.1109/TNS.2024.3365272.

García Alía, R., et al., 2018. LHC and HL-LHC: Present and future radiation environment in the high-luminosity collision points and RHA implications. IEEE Trans. Nucl. Sci. 65 (1), 448–456. http://dx.doi.org/10.1109/TNS.2017.2776107.

Girard, S., et al., 2013. Radiation effects on silica-based optical fibers: Recent advances and future challenges. IEEE Trans. Nucl. Sci. 60 (3), 2015–2036. http://dx.doi.org/10.1109/TNS.2012.2235464.

Girard, S., et al., 2018a. Growth and decay kinetics of radiation-induced attenuation in bulk optical materials. IEEE Trans. Nucl. Sci. 65 (8), 1612–1618. http://dx.doi.org/10.1109/TNS.2017.2778318.

Girard, S., et al., 2018b. Recent advances in radiation-hardened fiber-based technologies for space applications. J. Opt. 20 (9), 093001. http://dx.doi.org/10.1088/2040-8986/aad271.

Girard, S., et al., 2019. Overview of radiation induced point defects in silica-based optical fibers. Rev. Phys. 4, 100032. http://dx.doi.org/10.1016/j.revip.2019.100032.

Harb, J., et al., 2022. Femtosecond direct laser writing of silver clusters in phosphate glasses for x-ray spatially-resolved dosimetry. Chemosensors 10 (3), 110. http://dx.doi.org/10.3390/chemosensors10030110.

Holzer, E.B., et al., 2012. Beam loss monitoring for LHC machine protection. Physics Procedia 37, 2055–2062.

Huang, D., Hsu, S.-M., 2011. Radio-photoluminescence glass dosimeter (RPLGD). In: Advances in Cancer Therapy. IntechOpen, pp. 553–568. http://dx.doi.org/10.5772/23710.

Knežević, Z., et al., 2011. Characterisation of RPL and TL dosimetry systems and comparison in medical dosimetry applications. Radiat. Meas. 46 (12), 1582–1585. http://dx.doi.org/10.1016/j.radmeas.2011.05.042.

Knežević, Z., et al., 2013. Photon dosimetry methods outside the target volume in radiation therapy: Optically stimulated luminescence (OSL), thermoluminescence (TL) and radiophotoluminescence (RPL) dosimetry. Radiat. Meas. 57, 9–18. http://dx.doi.org/10.1016/j.radmeas.2013.03.004.

Kurobori, T., 2018. Performance characterisation of a real-time fiber dosimetry system using radiophotoluminescent glasses. Japan. J. Appl. Phys. 57 (10), 106402. http://dx.doi.org/10.7567/JJAP.57.106402.

Kurobori, T., et al., 2010. The role of silver in the radiophotoluminescent properties in silver-activated phosphate glass and sodium chloride crystal. Opt. Mater. 32 (9), 1231–1236. http://dx.doi.org/10.1016/j.optmat.2010.04.004.

Lerner, G., et al., 2023. Analysis of the radiation field generated by 200-MeV electrons on a target at the CLEAR accelerator at CERN. IEEE Trans. Nucl. Sci. 70 (8), 1572–1579. http://dx.doi.org/10.1109/TNS.2023.3252808.

McKeever, S.W., 2022. A course in Luminescence Measurements and Analyses for Radiation Dosimetry. Wiley and Son.

McKeever, S., Sholom, S., Shrestha, N., 2019. Observations regarding the build-up effect in radiophotoluminescence of silver-doped phosphate glasses. Radiat. Meas. 123, 13–20. http://dx.doi.org/10.1016/j.radmeas.2019.02.009.

McKeever, S., et al., 2020. Build-up of radiophotoluminescence (RPL) in Ag-doped phosphate glass in real-time both during and after exposure to ionizing radiation: A proposed model. Rad. Meas. 132, 106246. http://dx.doi.org/10.1016/j.radmeas.2020.106246.

Meyer, A., et al., 2023. Simulation and optimization of optical fiber irradiation with X-rays at different energies. Radiation 3 (1), 58–74. http://dx.doi.org/10.3390/radiation3010006.

Miyamoto, Y., et al., 2011. Radiophotoluminescence from silver-doped phosphate glass. Radiat. Meas. 46 (12), 1480–1483. http://dx.doi.org/10.1016/j.radmeas.2011.05.048.

Morana, A., et al., 2020. Extreme radiation sensitivity of ultra-low loss pure-silica-core optical fibers at low dose levels and infrared wavelengths. Sensors 20 (24), 7254. http://dx.doi.org/10.3390/s20247254.

Okada, G., et al., 2021. TSL/OSL/RPL automated and integrated measurement system (TORAIMS). Sensors Mater. 33 (6(4)), 2117–2128. http://dx.doi.org/10.18494/SAM.2021.3327.

Okada, G., et al., 2023. Recent advances in radiophotoluminescence materials for luminescence dosimetry. Japan. J. Appl. Phys. 62 (1), 010609. http://dx.doi.org/10.35848/1347-4065/ac9023.

Pramberger, D., et al., 2022. Characterization of radio-photo-luminescence (RPL) dosimeters as radiation monitors in the CERN accelerator complex. IEEE Trans. Nucl. Sci. 69 (7), 1618–1624. http://dx.doi.org/10.1109/TNS.2022.3174784.

Sholom, S., McKeever, S.W., 2020. High-dose dosimetry with Ag-doped phosphate glass: Applicability test with different techniques. Radiat. Meas. 132, 106263. http://dx.doi.org/10.1016/j.radmeas.2020.106263.

Spiezia, G., et al., 2011. The LHC radiation monitoring system - RadMon. Proc. Sci. 143, 1–12.

Vincke, H., et al., 2007. Response of alanine and radio-photo-luminescence dosemeters to mixed high-energy radiation fields. Radiat. Protect. Dosim. 125 (1–4), 340–344. http://dx.doi.org/10.1093/rpd/ncm157.

Vinke, H., Trummer, J., 2014. Apparatus and method for determining a dose of ionizing radiation. WO 2014/161732 A1, CH-1211 Geneva 23 (CH).

Wesolowska, P.E., et al., 2017. Characterization of three solid state dosimetry systems for use in high energy photon dosimetry audits in radiotherapy. Radiat. Meas. 106, 556–562. http://dx.doi.org/10.1016/j.radmeas.2017.04.017.

Yamamoto, T., 2011. RPL dosimetry: Principles and applications. AIP Conf. Proc. 1345 (1), http://dx.doi.org/10.1063/1.3576169.

Yanagida, T., et al., 2022. A review and future of RPL dosimetry. Radiat. Meas. 106847. http://dx.doi.org/10.1016/j.radmeas.2022.106847.

Yokota, R., Imagawa, H., 1967. Radiophotoluminescent centers in silver-activated phosphate glass. J. Phys. Soc. Japan 23 (5), 1038–1048. http://dx.doi.org/10.1143/JPSJ.23.1038.